Understanding the effect of Ni-substitution on the oxygen evolution reaction of (100) IrO_2 surfaces

Gaëtan Buvat [a, g], Mohammad J. Eslamibidgoli [a, b, f], Tianjun Zhang [c], Sagar Prabhudev [a, d], Azza Hadj Youssef [a], Andreas Ruediger [a], Sébastien Garbarino [e], Gianluigi A. Botton [d], Peng Zhang [c], Michael Eikerling [f], Daniel Guay [a *]

[a] Institut national de la recherche scientifique, Énergie, matériaux et télécommunications, 1650 Lionel-Boulet Boulevard, Varennes, QC J3X 1S2, Canada

[b] Department of Chemistry, Simon Fraser University, 8888 University Drive, Burnaby, BC V5A 1S6, Canada

[c] Department of Chemistry, Dalhousie University, 6274 Coburg Road, Halifax, NS B3H 4R2, Canada

[d] Department of Materials Science and Engineering, McMaster University, Hamilton, ON L8S 4L8, Canada

[e] PRIMA Québec, 505 de Maisonneuve Boulevard West, Montreal, QC H3A 3C2, Canada

[f] Theory and Computation of Energy Materials (IEK-13), Institute of Energy and Climate Research, Forschungszentrum Jülich GmbH, 52425 Jülich, Germany.

[g] Institut d'Electronique, de Microélectronique et de Nanotechnologies, Université de Lille, CNRS, Centrale Lille, Université Polytechnique Hauts-de-France, UMR 8520 - IEMN, F-59000 Lille, France

* To whom correspondence should be send: daniel.guay@inrs.ca

Abstract

The electrolysis process of water is impeded by the slow kinetics of the oxygen evolution reaction (OER). While iridium oxide (IrO_2) is considered as one of the most efficient metal catalyst for the OER, the adsorption of the OER intermediates at the IrO_2 surface is not optimal, the *OH intermediate being too strongly adsorbed. The substitution of iridium substitution by another metal cation is then a common strategy to improve the catalytic activity. A combined computational and experimental approach was followed to elucidate the fundamental effect of nickel on the OER activity of (100)-oriented IrO_2. To achieve this, (100)-oriented $Ir_{1-x}Ni_xO_2$ model surfaces were synthesized by pulsed laser deposition (PLD). Detailed structural and chemical characterizations were performed by XRD, TEM, AFM and XAS. The composition of the film was varied between 0 and 15 at.%, which is the solubility limit for the substitution of iridium by nickel atoms in (100)-oriented $Ir_{1-x}Ni_xO_2$. All electrochemical characterizations were performed in an alkaline electrolyte, in which nickel dissolution is not observed by XPS. The current density recorded at +1.6 V (*vs.* RHE) was increased from 35 to 348 µA cm^{-2}_{ox} between IrO_2 to $Ir_{0.85}Ni_{0.15}O_2$. DFT calculations showed that the energy diagram of the OER intermediates was modified by the substitution of iridium by nickel atoms through a ligand effect. Also, it was found that iridium is the active site for low nickel content, whereas nickel is the most active site when its concentration reaches 15 at.%.

Keywords

Oxygen evolution reaction, iridium oxide, nickel oxide, pulsed laser deposition, DFT calculation

1. Introduction

Hydrogen is an ideal and viable energy carrier for storing intermittent renewable energy from solar and wind power. As a fuel for power generation in fuel cells, hydrogen is a central component of current efforts to defossilize the global economy. However, nowadays, most of the hydrogen production is done by reforming hydrocarbons, which releases CO_2.[1-3] An environmentally benign alternative is to produce hydrogen by water electrolysis using green electricity, but this technology is obstructed by the sluggish oxygen evolution reaction (OER) at the anode side. Indeed, as the reaction involves the transfer of four electrons and protons, it exhibits a slow intrinsic kinetics and requires highly effective electrocatalytic materials to proceed at sufficient rate.[4] Iridium oxide appears to be the most suitable electrocatalytic material, as it combines high electrocatalytic activity with excellent stability.[5, 6] However, the high cost and scarcity of this metal jeopardize the large-scale adoption of water electrocatalysis. It is thus necessary to lower the OER overpotential for iridium-based catalysts while at the same time decreasing the Ir loading.[7] One possible approach that comes to mind is to increase the mass-specific surface area by scaling down Ir-based electrocatalysts to the size of nanoparticles.[8] Another approach is to enhance the intrinsic electrocatalytic activity of iridium oxide by alloying or doping with metallic components. It is vital to understand the OER at the atomistic scale in order to direct the synthetic efforts to this effect.

The Eley-Rideal (ER)-type and Langmuir-Hinshelwood (LH)-type adsorbate evolution mechanisms (AEM) are the two commonly accepted paths for the OER in acidic environments.[9] The distinction between the former (known as acid-base OER) and the latter (known as direct coupling OER) lies in the step for the O-O bond formation. Under aqueous conditions, the OER reaction cycle is triggered by the formation of metal hydroxide

intermediates (MOH), which are then transformed to metal-oxide species (MO). The formation of dioxygen from MO may occur through two distinct pathways. Either two MO centers are engaged, immediately splitting off dioxygen, or one MO intermediate combines with water to produce a hydro-peroxide species, which decomposes under dioxygen release. The nature of the OER mechanism is largely dependent on the type and structure of the catalyst. Both ER- and LH-type OER reactions entail four stages, beginning with the conversion of adsorbed OH (OH*) to O*, which results in metal site oxidation.

Because the ER-type AEM mechanism assumes single metal cation active sites, O* undergoes nucleophilic attack by an active initial water molecule in the second step, resulting in the production of OOH*. In the third step, OOH* is further oxidized to OO*, which is then released as O_2 in the final step, giving a free surface site for the following cycle, which begins with the adsorption of another water molecule. In contrast, the LH-type AEM process implies two neighboring metal cation active sites. As a result, OO* is generated between two O* species in the second stage by the direct connection of two near oxidized surface metal sites. The ER-type mechanism has been reported for Ru-based catalysts, while LH-type mechanisms have been described for Co-based catalysts.[4, 10] All steps in AEM pathways are assumed to be proton-coupled electron transfer (PCET). The OER overpotential in the RHE scale becomes pH-independent for catalysts that prefer these pathways, as observed for Ir oxide catalysts.[11]

Density Functional Theory (DFT) studies have shown that the adsorption of the intermediates on the IrO_2 surface is not optimal. Indeed, the metal oxide surface strongly binds the *OH intermediate, resulting in an OER overpotential that could be further reduced if the binding energy of the *OH intermediate could be decreased.[12] As the active metal's electronic state and band structure impact the adsorption energy of intermediates, one strategy to tailor the adsorption energy of the OER intermediates is to modify the electronic structure

of IrO_2. An efficient method, as previously investigated for the synthesis of Pt-based alloy catalysts for the oxygen reduction reaction, is the preparation of $Ir_{1-x}M_xO_2$-based catalyst, with M as a metallic element.[13-15] Indeed, in a previous joint experimental-computational study, well-defined (100) surface of $Ir_{1-x}M_xO_2$ prepared by Pulsed Laser Deposition (PLD) has identified nickel as the optimal candidate to substitute partially iridium. Along with lowering the precious metal content, replacing iridium by nickel allows for a weaker binding of the *OH intermediate.[16]

Alloys of nickel mixed with iridium have been the subject of numerous studies in the literature. Indeed, various systems have been investigated, including IrNi bimetallic nanoparticles,[17-20] $IrNi_x$-IrO_x core-shell nanoparticles,[21, 22] Ir-Ni binary oxide,[23, 24] thermally prepared Ir-Ni mixed oxide thin films,[25] and also the synthesis of an IrO_2 shell on an Ir-Ni core by a galvanic replacement process.[26, 27] Another avenue investigated was the preparation of Ir-Ni-based oxide composites, utilizing the strong interaction of the support to enhance the catalytic properties, such as nickel electrodeposition on polycrystalline and oriented iridium surfaces,[28] pulsed-electrodeposition of Ir-Ni oxides,[29] and deposition of isolated iridium atoms on a NiO matrix.[30] Finally, the substitution of iridium with cobalt and nickel inIrO_2 rutile structure nanoparticles was investigated.[31]

However, most of the electrocatalytic materials described above were synthesized at the nano-scale and subsequently oxidized thermally and/or electrochemically, sometimes followed by an acid leaching treatment, resulting in a variety of surface morphologies. While these preparation methods are viable for the development of durable catalysts, using them to elucidate the OER mechanisms behind performance improvements is challenging. Moreover, when computational work is involved, the typical slab-like geometries of regularly spaced atoms with distinct and well-defined surface terminations employed for DFT calculations may deviate from the real structure/surface morphologies examined in the experiments. Therefore,

the comparison of experimental and theoretical results can be tricky. In addition, most studies have characterized the activity for the OER in an acidic environment, in which nickel is leached. Although the vacant site left by nickel dissolution has been shown to enhance the OER activity,[22] the mechanistic role of nickel in enhancing the electrocatalytic activity of IrO_2 in alkaline solution, in which Ni dissolution does not occur, has not been determined.

To fill this gap, using pulsed laser deposition, well defined $Ir_{1-x}Ni_xO_2$ surfaces were prepared along the (100) crystallographic orientation, owing to its superior catalytic properties for the OER compared to IrO_2's most thermodynamically stable (110) plane.[32] The electrochemical behaviour of (100)-oriented $Ir_{1-x}Ni_xO_2$ surfaces was characterized in alkaline media. DFT calculations, in addition to extensive structural and chemical analyses, were performed to better understand the role of nickel when mixed with iridium oxide, which exhibits a significant improvement in the OER activity.

2. Experimental conditions

2.1. Thin film synthesis

Iridium-nickel mixed oxide films with (100) orientation were grown by reactive pulsed-laser deposition (PLD) in a custom-made turbo-pumped stainless-steel vacuum chamber with a vacuum base pressure of 10^{-5}Torr. A KrF laser beam (248 nm; pulse width of 17 ns) was focused on an iridium target (99.99%, Kurt J. Lesker Company) partially covered by a nickel foil (99.994% from Alfa Aesar). A 6 $J.cm^{-2}$ laser fluence was used with a repetition rate of 20 Hz and 60,000 pulses. The target was kept in a continuous rotational and translational motion for uniform ablation. The substrates used were commercial (100)-oriented $SrTiO_3$ crystals (10 × 10 × 0.5 mm, epi polished from MTI Corporation) that were kept in continuous rotation. During deposition, the substrates were heated to 600°C and oxygen pressure was 100 mTorr. The distance from the target to the substrates was

maintained at 5.5 cm. Before deposition, the substrates were cleaned by sonication in acetone (15 min) and in isopropanol (15 min), and then dried under an argon stream.

2.2. Thin film characterization

The films' crystallographic orientation was analyzed by x-ray diffraction using a four-circle x-ray diffractometer (PANalyticalX'pert Pro diffractometer, with a Cu $K\alpha_{1+2}$ radiation). Out-of-plane orientation was measured in the $\theta/2\theta$ Bragg-Brentano mode (step size = 0.016°/step and counting time = 1 s/step). The epitaxy relationship was studied *via* x-ray pole figure measurement that were obtained from φ-scan, with φ varying from 0 to 360 degrees at 1°/step with 0.5 s/step, performed at different χ inclination, with χ varying from 0 to 85 degrees at 1°/step with 0.5 s/step. The thickness of each film was measured by x-ray reflectivity measurements conducted by varying the incident angle from 0.1° to 4° every 0.005° (1 s/step).

The chemical composition was measured by energy-dispersive x-ray spectroscopy (EDX) with a Bruker Quantax detector on a Scanning Electron Microscopy Tescan Vega3 LMH.

X-ray photoelectron spectroscopy (XPS) measurements were carried out with a VG Escalab 220i-XL spectrometer using monochromatic Al Kα radiation (1486.6 eV). The analyzed sample area measured was 250 x 1000 µm². The analysis chamber pressure was roughly 1.10^{-9} mbar. Scan survey spectra were recorded using a constant pass energy of 100 eV, whereas high-resolution spectra of Ir 4f and Ni 2p core levels were collected with a constant pass energy of 20 eV at $\theta = 0°$ take-off angle (angle between the surface normal and the detection direction). The binding energy scale was calibrated from the hydrocarbon contamination using the C 1s peak at 284.6 eV. All spectra were analyzed using CasaXPS

software (Casa Software Ltd, 2005). Core peaks were analyzed using a nonlinear Shirley-type background.

X-ray Absorption Spectroscopy (XAS) measurements were performed using the Sector 20-BM beamline of the Advanced Photon Source at Argonne National Laboratory (Argonne, IL). The beamline was equipped with a double-crystal Si(111) monochromator. A 12-element Ge fluorescence detector was used to collect spectra of the Ir L3 and Ni K edges. The energy was calibrated according to the absorption edge of a pure Ir powder or Ni foil, as appropriate. Data processing and fitting were performed using WinXAS and Analyzer v0.1 software, with scattering paths generated by FEFF8.[33, 34] S02 values for Ir (0.92) and Ni (0.71) were obtained by fitting Ir powder and Ni foil, respectively.

Film thickness was checked using a FEI-Titan 80-300 cubed TEM operated at 300 kV in scanning TEM mode (STEM). The microscope is equipped with a high-brightness Schottky electron source, aberration correctors for both probe-forming and image-forming lenses, and a high-resolution Gatan-K2 direct electron detector. A focused ion beam (FIB) technique was used to carefully lift out ultra-thin cross-sections of the (Ir,Ni)O_2/$SrTiO_3$ samples, which in certain cases required further surface cleaning with low energy Ar milling. Detailed elemental mapping was carried out using electron energy loss spectroscopy (EELS) involving a recording of EELS spectra at every pixel while recording the high angle annular dark field (HAADF) image and subsequent signal extraction of the Ni-L2,3 edges and signal quantification using the built-in quantification in the Gatan Digital Micrograph software.

The films' surface morphologies were obtained through atomic force microscopy (AFM Smart SPM1000-AIST-NT Inc.), with images acquired in intermittent mode. An AIST-NT Smart system in an acoustic enclosure on an active anti-vibration support was operated with an aluminum coated n-type silicon cantilever (HQ:NSC15/Al BS, MikroMasch) with

nominal values (tip radius of 8 nm, a force constant of 40 N/m, and a resonance frequency of 325 kHz).

2.3. Electrochemical characterization

Electrochemical measurements were carried out in a custom made 4 mL one-cell compartment, described previously.[35] A gold wire located outside the cell and in contact with the thin film was used as the current collector. A platinum mesh, which was previously flame-annealed and quenched in water, was used as the counter-electrode. The reference used was an Hg/HgO electrode separately located in an external compartment and connected to the main cell via a Luggin capillary.

After each thin film characterization, the reference electrode's potential was calibrated against a hydrogen electrode using the same electrolyte from the same batch, and then converted to the RHE scale. The electrolyte used was sodium hydroxide (NaOH99.99%, Alfa Aesar) at a concentration of 0.1 M. The electrolyte was purged for 10 minutes with high-purity argon before measurement. Subsequently, a constant argon flow was maintained during characterization. Ultrapure water (Millipore Gradient, MilliQ, resistivity ≥ 18.2 MΩ cm) was used to prepare the electrolyte.

Prior to each measurement, all glassware was cleaned by overnight immersion in an aqueous H_2SO_4/$KMnO_4$ solution. Finally, after rinsing, the glassware was boiled in a nitric acid solution followed by several boils in MilliQ water. All measurements were carried out with a BioLogic VSP potentiostat equipped with a low-current option, controlled by EC-Lab software. The exposed geometric surface area was 0.28 cm^2. The electrochemically active surface area (EASA) was obtained by determining the double-layer capacitance in a potential region where there is no Faradaic reaction, in accordance with the method reported by

McCrory *et al.*[36] The EASA was calculated by dividing the double-layer capacitance by a specific capacitance of 0.080 mF cm^{-2}.

2.4. DFT calculation

Vienna Ab Initio Simulation Package (VASP) was used to perform the DFT calculations.[37-40] All calculations were based on the Projector Augmented Wave (PAW) method.[41] According to this method, core electrons were kept frozen and replaced by pseudopotentials (Ir, M, O, H), and valence electrons (Ir: 5d76s2; O: 2s2 2p4; H: 1s1) were expanded in a plane wave basis set with a kinetic energy cut-off of 400 eV. The ionic relaxation loop terminates when the forces on all atoms are less than 0.01 eV/Å. Exchange-correlation effects were incorporated within the generalized gradient approximation (GGA), using the functional by Perdew, Burke, and Ernzerhof (PBE).[42] The Brillouin zone was sampled using the Monkhorst−Pack[43] system, using 6 × 6 × 8 k-points for the bulk and 4 × 4 ×1 k-points for the slab calculations.

3. Results and discussion

3.1. Thin film synthesis of (Ir,Ni)O_2

The Ir – Ni – O system was explored in all composition ranges by varying the iridium/nickel target surface exposed to the PLD beam. The films' structure was characterized by θ-2θ x-ray diffraction, and the determination of the atomic ratio iridium/nickel was measured by EDX. All XRD patterns show the reflections of the (h00) $SrTiO_3$ substrate at *ca.* 2θ = 23 and 46°, labelled in black in Figures 1A and S1. For a nickel content between 0 and 15 at.%, the peak present at *ca.* 2θ = 40° is attributed to the (200) plane of IrO_2. However, we notice a weak reflection of the (110) IrO_2 plane (2θ = 28°) in the film composed of 15 at.% nickel. On one hand, the ratio intensity [$A_{(110)}/(A_{(110)}+A_{(200)})$] of *ca.* 0.9% may be considered negligible ($A_{(hkl)}$ being the integrate surface under the (hkl) peak); but on the other hand, it

indicates a limit to the substitution of iridium with nickel and together, preserving the (100) orientation. Indeed, as shown in Figure S1, the XRD patterns of the films with a nickel content between 15 and 40 at.% present the (200) and (110) orientations of IrO_2. Moreover, for a composition of 50 at.% nickel, a new reflection was observed at *ca.* 2θ = 43°, corresponding to the (200) plane of NiO. Films with a rich nickel composition (> 60 at.%) present only the (200) NiO peak. These results indicate that the (100) orientation of IrO_2 is preserved only when the nickel content is low, and that the (110) orientation of IrO_2 start to appear as the Ni content exceed 15 at.%. Indeed, the (110) plane of IrO_2 is the most thermodynamically stable facet (surface energy $\gamma(110) < \gamma(100)$[44]); and a small perturbation, such as substitution of iridium by nickel atoms, appears to turn on the overall system's energy balance. Also, IrO_2 crystallizes in a tetragonal structure with $a = b$ = 4.4983 Å and c = 3.1544 Å, whereas the structure of NiO is cubic with a = 4.1771 Å. The difference in the crystal structure of both oxides explains the presence of a bi-phasic film for intermediate nickel content. In the remaining of the work, we will focus solely on the (100) iridium-rich oxide with nickel contents between 0 and 15 at.%.

A detailed view of the (200) IrO_2 reflection of the latter films is depicted in Figure 1B, and the out-of-plane lattice parameters a are summarized in Table1. The lattice parameter decreases as nickel content increases, and the evolution of the out-of-plane parameter is consistent with the formation of a solid solution, as will be presented in the section on EXAFS characterization.

To evaluate further the in-plane epitaxy relationship, x-ray diffraction pole figures along the <110> direction of IrO_2 have been recorded (Figures S2). All pole figures show spots oriented at χ 45° with respect to the out-of-plane <100> direction of IrO_2, which confirm the epitaxial growth of (100) single crystals. However, all films exhibit a signature with 12 spots instead of four for the $SrTiO_3$ substrate, whose intensity varies with the Ni content. This

is indicative that there are two domains of (100) IrO_2 single crystals with different orientations with respect to the substrate. These results are in line with our earlier work, showing that (100) IrO_2 on (100) $SrTiO_3$ grows along two commensurate domains oriented in-the-plane at ±14° (7b × 5c) and ± 45° (5b × 7c) with respect to the substrate.[45]

To make sure that nickel is homogeneous distributed in IrO_2, a detailed compositional characterization was performed by EELS. Figure S3 illustrates the elementary mapping of nickel in the thin film region. The distribution of nickel is homogeneous all over the film, as it was expected from the slight decrease of the lattice parameters measured by XRD.

The film thickness was measured by x-ray reflectivity (Table 1), where the thickness of the films decreases as nickel content increases. This tendency comes from the different ablation rates of nickel and iridium.[46] In addition, the HAADF-STEM image in Figure S4 provides a reliable estimation of film thickness at about 80 nm, close with the XRR measurements.

Finally, the thin films' surface topography was observed by AFM, as seen in Figure S5. Grains of $(Ir,Ni)O_2$ present a rice shape, as previously observed,[45] and their orientations with respect to the substrate are in line with the pole figure measurements. Also, the RMS roughness (Table 2) decreases with nickel content, from 1.67 nm to 0.93 nm with 0 at.% and 15 at. % nickel, respectively. These low values highlight the benefit of using PLD to produce a smooth film, leading to a proper way to measure the intrinsic catalytic properties.

3.2. Electrochemical characterization

The electrocatalytic performances of epitaxial (100) $(Ir,Ni)O_2$ films for the oxygen evolution reaction were characterized by near steady-state cyclic voltammetry in 0.1M NaOH. The current density was normalized by the electrochemically active surface area (EASA), as described in the experimental section and summarized in Table 2.The EASA values, as well

as the roughness factor from AFM measurements, decrease when nickel content increases. Also, the EASA values are close to the geometrical surface area (0.28 cm^2), in agreement with the low RMS roughness (< 1.7 nm). This emphasizes the flatness of the films prepared by PLD and dismisses the contribution of the texture that could have varied with the film's composition. The measured electrochemical performances are then relative to the material's intrinsic properties.

Figure 2A illustrates the catalytic behavior of the (100) (Ir,Ni)O_2 films after they have reached a steady-state, and shows that the current density is influenced by nickel content; the higher the nickel content, the higher the electrochemical performances. The electrocatalytic activity of (100)-oriented NiO film substituted with 20 at.% of iridium atom was compared (100)-oriented $Ir_{0.85}Ni_{0.15}O_2$ film in Figure S6). The OER activity of the former film is negligible compared to the latter film, emphasizing that the substitution of a small fraction of iridium by nickel atom in the rutile structure of IrO_2 is key to increasing the OER activity of the material. The inset in Figure 2A and Table 2 shows the current density measured at 1.6V (*vs.* RHE) of the Ir-rich (100) (Ir,Ni)O_2 films. With 15 at.% nickel, the current density is 348 $\mu A.cm^{-2}{}_{ox}$, which is 10 times higher than that of the IrO_2 parent compound.

Figure 2B displays a zoom of the IrO_2 and $Ir_{0.85}Ni_{0.15}O_2$ CV in the potential region before the OER take place. The sample with nickel shows redox waves in the forward and backward sweeps at *ca.* 1.45 V *vs.* RHE. This signature is characteristic of nickel oxidation-reduction,[47] as pure iridium film does not exhibit any redox peak in the potential range. However, these redox reactions are not occurring in the same potential range compared to pure nickel (average position between the forward and backward scan at around 1.33 V *vs.* RHE), and must be relative to the chemical/structural environment around nickel.[47, 48]

Figure S7 presents the cyclic voltammetry (scan rate: 100 mV s^{-1}) of $Ir_{0.85}Ni_{0.15}O_2$ and IrO_2 films. On IrO_2, a very broad redox peak was observed at 0.9 V *vs.* RHE, assigned to the Ir^{3+}/Ir^{4+} redox reaction, which is not seen in the Ni-substituted sample.

Figure 3 presents the Tafel plot measured via near steady-state cyclic voltammetry at a low scan rate of 1 $mV.s^{-1}$, and calculated by averaging the forward and backward sweeps. The overpotential measured at 10 $\mu A.cm^{-2}{}_{ox}$ decreases from 0.341 V to 0.314 V and 0.300 V for 0, 4 and 15 at.% nickel, respectively (see Table 2). The overpotential is more than 40 mV lower for (100) $Ir_{0.85}Ni_{0.15}O_2$ than (100) pure IrO_2, indicating the beneficial effect of partially substituting Ir by Ni atoms in the rutile structure of IrO_2.[16] As mentioned above, for Ni content larger than 15 at.%, a non-negligible fraction of the film grows along the (110) direction, and the electrochemical properties of these samples were not investigated.

The (100) IrO_2 film has a slope of 56 $mV.dec^{-1}$, consistent with previous results.[32] However, the slope of the 15 at.% nickel film is 40 $mV.dec^{-1}$. Interestingly, this value is close to the Tafel slope found for Ni-based catalyst, which ranges also around 40 $mV.dec^{-1}$.[47-49] This change of Tafel slope with the introduction of Ni atoms into the crystalline structure of rutile IrO_2 suggests a possible role for nickel as an active site.

3.3. Geometric and electronic structure characterization

A more complete picture of the films' structure and surface electronic configuration is required to understand the effect of Ni substitution in the IrO_2 rutile structure. At this point, it seems relevant to investigate the local environment of the iridium and nickel atoms. For this purpose, a detailed characterization was conducted by x-ray absorption spectroscopy, and investigation of the local structure and coordination environment around the iridium and nickel sites was carried out by extended x-ray absorption fine structure (EXAFS). Figure 4A

shows the Fourier Transformed EXAFS (FT-EXAFS) spectra for the iridium signal extracted from the L3 edge.

The first peak below 2 angstroms for all the iridium-based oxide samples represents the Ir–O bond, whereas the double peak in the region of 2–3 angstroms may be assigned to the Ir–O bond tail. Further peaks above 3 angstroms were assigned to the long-distance Ir–Ir bond in iridium oxide. Table 3 and Figure S8 show the results of the fitting of the FT-EXAFS. According to these results, the coordination number (CN) of the Ir–O bond in the pure IrO_2 sample is 6.0 and the bond distance is 1.95Å; this is in line with the octahedral environment of iridium in the rutile structure. Although the Ir–O distance is shorter than expected (1.98Å), it is in accordance with our previous work and calculations due to the small orthorhombic distortion induced by the $SrTiO_3$ substrate.[45] The coordination numbers for the mixed oxides decreased slightly, whereas the bond distance remained relatively the same as that of IrO_2.

We also studied the geometric environment around the nickel. Figure 4B presents the FT-EXAFS results. The first peak below 2 angstroms of the spectra represents the Ni–O bond, whereas the peak around 3 angstroms may be assigned to the long-distance Ni–Ni bond. Table 3 and Figure S9 present the results of the fitting. These findings show that the Ni–O bond's coordination number decreases (from 5.7 to 5.0) as the Ni content increases; however, the bond distance for all samples is close to 2.03 angstroms. The local Ir/Ni–O environment from XAS seems to conclude that nickel atoms do not adopt the signature of a nickel oxide (NiO), where the first shell coordination of nickel is 6, with a bond distance of 2.10 angstroms. Consequently, nickel atoms are located in the center of the typical octahedral sites found in rutile IrO_2, and the original [IrO_6] geometric structure is not disrupted by the addition of nickel.

We performed complementary x-ray photoelectron spectroscopy measurements to investigate the chemical nature of the (Ir,Ni)O_2 thin films' surface. Figure 5A displays the Ir 4f region of a native surface of the films (Figure S10A after OER), presenting the usual asymmetric double-peak shape ($4f_{7/2}$ and $4f_{5/2}$). The peak binding energy (62.0 eV) is similar to that for iridium oxide, and there is no metallic iridium at the surface, whose binding energy is expected at *ca.* 60.9 eV.[50] The asymmetric peak is representative of the final state screening and the metallic behavior of IrO_2.[51] As we observed from the spectra, the binding energy of the IrO_2 sample occurred at 61.9 eV, which corresponds to a +4 oxidation state of iridium.[50] When iridium was substituted for nickel, the peak position occurs at a lower binding energy of 61.8 eV, indicative of a change in the oxidation state of iridium from +4 to +3.

Figure 5B shows the XPS spectra of as-deposited film in the Ni 2p region and Figure S10B after OER. The spectrum has the common double-peak $2p_{3/2}$ and $2p_{1/2}$, along with their satellite peaks. The main $2p_{3/2}$ peak is positioned at *ca.* 855.5 eV with a second contribution at *ca.* 853.5 eV. The line shape of the Ni 2p peaks are then characteristic of an oxidation state of +2/+3, and no metallic nickel is observed, whose binding energy is expected at *ca.* 852.6 eV.[52]

Lastly, the Ir/Ni ratio was quantified on the pristine samples and after the electrochemical characterization steps (see Table 4). The XPS survey spectra of both samples are shown in Figure S11. Compared to EDX measurements (Table 1), the surface appears richer in nickel than the bulk. In addition, there was no significant decrease in the Ir/Ni ratio after OER, which suggests that metal cations are not dissolved during the OER.

3.4. Discussion

In view of the observations provided above, the significant increase in $Ir_{1-x}Ni_xO_2$ activity raises questions regarding the role of nickel in the OER mechanisms. To gain a better grasp of this role, we carried out a series of DFT computations using different surface structures. The mechanism that governs the OER is influenced by the electronic structure of the catalyst, which determines the adsorption energies of OER intermediates. Based on the structural and physicochemical analyses described before, it was found that nickel atoms are dissolved and thus distributed homogeneously into the rutile structure of IrO_2 at a Ni concentration ≤ 15 at.%, while preserving the film's (100) surface structure.

Next, two (100) $Ir_{1-x}Ni_xO_2$ surfaces with nickel compositions were investigated, linked to the films prepared using PLD: one with a lower nickel content ($Ir_{0.94}Ni_{0.06}O_2$, Figure S12B), and another with a higher content ($Ir_{0.75}Ni_{0.25}O_2$, Figure S12C). Additionally, a third surface model, (100) IrO_2 (Figure S12A), was considered. For this, a four-layer slab with a rutile structure was constructed, with iridium atoms uniformly substituted by nickel atoms in the targeted compositions, in contact with a vacuum layer of about 15 Å.

Next, the surfaces with intermediate species (*O, *OH and *OOH) were optimized according to the OER mechanism (Figure S13),[12]

$$H_2O \rightarrow *OH_{ad} + H^+ + e^- \quad (1)$$

$$*OH_{ad} \rightarrow *O_{ad} + H^+ + e^- \quad (2)$$

$$H_2O + *O_{ad} \rightarrow *OOH_{ad} + H^+ + e^- \quad (3)$$

$$*OOH_{ad} \rightarrow * + O_2 + H^+ + e^- \quad (4)$$

The adsorption energies of the OER intermediates were calculated as,

$$\Delta E(*OH) = E(*OH) - E_{ref}(*) - [E(H_2O) - \tfrac{1}{2}E(H_2)] \quad (5)$$

$$\Delta E(*OOH) = E(*OOH) - E_{ref}(*) - [2E(H_2O) - 1.5E(H_2)] \quad (6)$$

$$\Delta E(*O) = E(*O) - E_{ref}(*) - [E(H_2O) - E(H_2)] \quad (7)$$

where $E_{ref}(*)$, E(*OH), E(*O), and E(*OOH) are the ground state energies of the slab and the slab with adsorbed *OH, *O, and *OOH intermediates, respectively; $E(H_2O)$ = -14.2239 eV and $E(H_2)$ = -6.7658 eV are the calculated DFT energies of H_2O and H_2 molecules in the gas phase.

The influence of nickel on the OER activity can be seen from the OER energy diagram, shown in Figure 6A-C, which corresponds to the energy required for each intermediate to be adsorbed on the catalyst surface. The black curve corresponds to an ideal catalyst, according to the computational hydrogen electrode,[53] for which the transition between the different OER intermediates requires the same energy (1.23 eV). The OER energy diagram of Figure 6A compares the adsorption energy of each intermediate at iridium site on the (100) surface of IrO_2, $Ir_{0.94}Ni_{0.06}O_2$ and $Ir_{0.75}Ni_{0.25}O_2$. On this site, each OER intermediate binds less strongly to the surface of the mixed oxides than pure iridium oxide. As shown in Figure 6D, the thermodynamic overpotential of both mixed oxide surfaces are closer to the apex of the volcano plot compared to pure IrO_2, and close to the thermodynamic overpotential of pristine NiO,[54] although there is not much difference between $Ir_{0.94}Ni_{0.06}O_2$ and $Ir_{0.75}Ni_{0.25}O_2$. The trends derived from the DFT calculations are in agreement with those established experimentally, where it has been shown that the activity for the OER increases in the order (100) IrO_2 < (100) $Ir_{0.94}Ni_{0.06}O_2$ < (100) $Ir_{0.75}Ni_{0.25}O_2$. However, the data of Figure 6A and 6D cannot account for the factor of 3 improvement of the OER current density at +1.60 V observed in Figure 2A when the Ni content is increased from 0.04 to 0.15.

The influence of nickel can originate from the combined effects responsible for modifying the catalytic properties of the iridium site: (i) a geometric effect due to the

expansion or shrinkage of the rutile structure, which induces a redistribution of the energy state close to the Fermi level, and (ii) a ligand effect that changes the chemical nature of the bond between atoms, and which is thus dependent on the electronic nature of the foreign atom. XRD and XAS characterizations have shown a decrease of the lattice parameters and the Ir–O interatomic distance, respectively, resulting in a compressive strain compared to IrO_2.The effect of a compressive strain on the catalytic properties for the OER is well documented. As an example, for perovskite structures, the beneficial effect of a lattice compression on the OER was attributed to a splitting and an asymmetric occupancy of the e_g orbital.[55-57] However, this effect is less likely to occur in rutile structures. Indeed, earlier works on IrO_2 have shown that strain-induced OER enhancement was negligible, because the strain does not break the symmetry around the adsorption site.[58] On the other hand, the presence of Ni modifies the d-band structure of surface Ir atoms. IrO_2 exhibits a metallic conductivity due to hybridized O 2p and Ir 5d electronic states in the valence band around the Fermi level.[59] On the other hand, the adsorbate-surface bond is formed by the coupling of adsorbate orbitals to the active site-projected d-band. Therefore, by knowing the electronic structure of the active site, the relative binding strength of the adsorbate can be, in principle, obtained. The presence of Ni modifies the d-band structure of surface Ir atoms due to both ligand and strain effects.[60] According to the d-band model, an upshift in the average energy of the d-states, also called the d-band center, relative to the Fermi level results in a stronger interaction between surface sites and adsorbates.[61] Indeed, as shown in Figure 7 for the computed d-projected density of states of surface Ir atoms, the d-band center down-shifts in the presence of Ni, resulting in weaker binding between the adsorbates and the surface Ir sites.

Furthermore, in order to isolate the strain effect from the ligand effect, DFT calculations were performed on a strained IrO_2 slab with the same level of compression as found experimentally in the $Ir_{0.75}Ni_{0.25}O_2$ mixed oxide but without any substitution of any Ir

atoms by Ni. In the calculation, the out of plane lattice parameter of the strained IrO_2 slab was 4.46 Å, instead of 4.51 Å for un-strained IrO_2. Chemisorption of the OER intermediates was calculated at the iridium site of the (100) surface (Figure 6B). The OER energy diagram reveals that strain alone has a negligible influence on the binding energy of the intermediates, with the chemisorption energy of each intermediate only reduced by 0.02 - 0.05 eV compared to pure IrO_2. This suggests that decreasing the Ir–O interatomic distance of the rutile structure does not significantly improve the OER activity. This is consistent with previous works on the strain effect in doped 4d and 5d late transition metal rutile oxides, which was found to be an order of magnitude lower than the ligand effect, with the effect being also dependent on the metal cation's chemical identity.[62]

Up to now, the effect of "doping" IrO_2 with Ni atoms to form (100) $Ir_{1-x}Ni_xO_2$ surfaces has focused on the Ir site of the slab. However, the CVs of Figure 2B clearly show peaks associated with the Ni^{+3}/Ni^{+4} redox transition at a potential less positive than the onset potential for the OER. Thus, the adsorption energy of the OER intermediates were computed at the nickel site of the (100) $Ir_{0.75}Ni_{0.25}O_2$ slab (Figure 6C and Figure 6D). On this surface, chemisorbed intermediates *OH and *OOH exhibit binding energies that more closely approach the values expected for an ideal catalyst. Indeed, the energy difference between the adsorption of *OOH and *OH was 2.48 eV for the (100) $Ir_{0.75}Ni_{0.25}O_2$ surface, very close to the energy difference of an ideal catalyst (2.46 eV).[12, 63] This suggests that Ni could be the active site in the (100) $Ir_{0.85}Ni_{0.15}O_2$ electrode that were investigated in the first part of this work.

4. Conclusion

A joint computational and experimental investigation of the activity of (100)-oriented $Ir_{1-x}Ni_xO_2$ layers was performed. It was shown that iridium atoms in the rutile structure can be

substituted by 15% nickel atoms without affecting the (100)-orientation of the electrode surface. Both DFT calculations and experimental data indicate that the OER characteristics of (100)-oriented $Ir_{1-x}Ni_xO_2$ are better than (100)-oriented IrO_2. The improved performance for the OER was observed in an alkaline electrolyte, in which Ni dissolution is minimal, as assessed by XPS investigation of the electrode surface before and after electrochemical characterization, and the current density at +1.6 V was increased from 35 to 348 $\mu A\ cm^2_{ox}$ between (100)-oriented IrO_2 and $Ir_{0.85}Ni_{0.15}O_2$. DFT calculations showed that the substitution of iridium by Ni atoms modifies favorably the adsorption energies of the intermediates involved in the OER through a ligand effect. At the iridium site, the thermodynamic overpotential of $Ir_{0.94}Ni_{0.06}O_2$ and $Ir_{0.75}Ni_{0.25}O_2$ are almost superimposed, which makes it difficult to explain the factor of 3 increase of the OER current between these two electrodes. At the iridium site, the beneficial effect of substituting iridium for nickel in the (100)-oriented $Ir_{1-x}Ni_xO_2$ electrodes saturates rapidly. This saturation effect is not observed at the Ni site and it is suggested that the active site of the electrode may change with the Ni content, iridium being the active site for a low nickel content (*ca.* Ni ≤ 4 at.%), while nickel is the active site when the Ni content reaches *ca.*15 at.%. A similar conclusion was reached for Fe-doped nickel bilayer hydroxides, the catalytic site being the doping iron atoms instead of Ni.[54, 64]

Supporting Information

The Supporting Information is available free of charge on the ACS Publications website.

S1, Structural evolution of $Ir_{1-x}Ni_xO_2$ thin films. S2, XRD pole figures of $(Ir,Ni)O_2$ thin films. S3, Ni distribution in IrO_2 by STEM-EELS. S4, HAADF-STEM of (100) $Ir_{0.85}Ni_{0.15}O_2$ film. S5, AFM of (100) $(Ir,Ni)O_2$ thin films. S6, OER activity of (100) $Ni_{0.80}Ir_{0.20}O$. S7, Voltammetry cyclic of (100) IrO_2 and (100) $Ir_{0.85}Ni_{0.15}O_2$ at 100 $mV.s^{-1}$. S8-S9, FT-EXAFS of

(100) (Ir,Ni)O_2 thin films. S10, XPS of (100) $Ir_{0.85}Ni_{0.15}O_2$ thin film. S11, XPS survey. S12, Crystalline rutile structures. S13, Adsorbate configurations.

Acknowledgement

This research was conducted as part of the Engineered Nickel Catalysts for Electrochemical Clean Energy project administered by Queen's University and supported by Grant No. RGPNM 477963-2015 under the Natural Sciences and Engineering Research Council of Canada (NSERC) Discovery Frontiers Program. This research used resources of the Advanced Photon Source, a User Facility operated for the US Department of Energy (DOE) Office of Science by Argonne National Laboratory and was supported by the DOE under contract no. DE-AC02-06CH11357 and the Canadian Light Source and its funding partners. Electron microscopy work was done at the Canadian Centre for Electron Microscopy a facility supported by the Canada Foundation for Innovation under the MSI program, NSERC and McMaster University.

References

1. Turner, J.A., *Sustainable Hydrogen Production*, Science, **2004**, 305(5686), 972-974
2. Chu, S.; A. Majumdar, *Opportunities and challenges for a sustainable energy future*, Nature, **2012**, 488(7411), 294-303
3. Buttler, A.; H. Spliethoff, *Current status of water electrolysis for energy storage, grid balancing and sector coupling via power-to-gas and power-to-liquids: A review*, Renewable and Sustainable Energy Reviews, **2018**, 82, 2440-2454
4. Reier, T.; H.N. Nong; D. Teschner; R. Schlögl; P. Strasser, *Electrocatalytic Oxygen Evolution Reaction in Acidic Environments – Reaction Mechanisms and Catalysts*, Adv. Eng. Mater., **2017**, 7(1), 1601275
5. Seh, Z.W.; J. Kibsgaard; C.F. Dickens; I. Chorkendorff; J.K. Nørskov; T.F. Jaramillo, *Combining theory and experiment in electrocatalysis: Insights into materials design*, Science, **2017**, 355(6321), eaad4998
6. Reier, T.; M. Oezaslan; P. Strasser, *Electrocatalytic Oxygen Evolution Reaction (OER) on Ru, Ir, and Pt Catalysts: A Comparative Study of Nanoparticles and Bulk Materials*, ACS Catal., **2012**, 2(8), 1765-1772
7. Bernt, M.; A. Siebel; H.A. Gasteiger, *Analysis of Voltage Losses in PEM Water Electrolyzers with Low Platinum Group Metal Loadings*, J. Electrochem. Soc., **2018**, 165(5), F305-F314
8. Povia, M.; D.F. Abbott; J. Herranz; A. Heinritz; D. Lebedev; B.-J. Kim; E. Fabbri; A. Patru; J. Kohlbrecher; R. Schäublin; M. Nachtegaal; C. Copéret; T.J. Schmidt, *Operando X-ray characterization of high surface area iridium oxides to decouple their activity losses for the oxygen evolution reaction*, Ener. Env. Sci., **2019**, 12(10), 3038-3052

9. Mavros, M.G.; T. Tsuchimochi; T. Kowalczyk; A. McIsaac; L.-P. Wang; T.V. Voorhis, *What Can Density Functional Theory Tell Us about Artificial Catalytic Water Splitting?,* Inorg. Chem., **2014**, 53(13), 6386-6397

10. Mattioli, G.; P. Giannozzi; A. Amore Bonapasta; L. Guidoni, *Reaction Pathways for Oxygen Evolution Promoted by Cobalt Catalyst,* J. Am. Chem. Soc., **2013**, 135(41), 15353-15363

11. Nakagawa, T.; C.A. Beasley; R.W. Murray, *Efficient Electro-Oxidation of Water near Its Reversible Potential by a Mesoporous IrOx Nanoparticle Film,* J. Phys. Chem. C, **2009**, 113(30), 12958-12961

12. Man, I.C.; H.-Y. Su; F. Calle-Vallejo; H.A. Hansen; J.I. Martínez; N.G. Inoglu; J. Kitchin; T.F. Jaramillo; J.K. Nørskov; J. Rossmeisl, *Universality in Oxygen Evolution Electrocatalysis on Oxide Surfaces,* ChemCatChem, **2011**, 3(7), 1159-1165

13. Escudero-Escribano, M.; K.D. Jensen; A.W. Jensen, *Recent advances in bimetallic electrocatalysts for oxygen reduction: design principles, structure-function relations and active phase elucidation,* Current Opinion in Electrochemistry, **2018**, 8, 135-146

14. Stamenkovic, V.R.; B.S. Mun; M. Arenz; K.J.J. Mayrhofer; C.A. Lucas; G. Wang; P.N. Ross; N.M. Markovic, *Trends in electrocatalysis on extended and nanoscale Pt-bimetallic alloy surfaces,* Nature Materials, **2007**, 6(3), 241-247

15. Greeley, J.; I.E.L. Stephens; A.S. Bondarenko; T.P. Johansson; H.A. Hansen; T.F. Jaramillo; J. Rossmeisl; I. Chorkendorff; J.K. Nørskov, *Alloys of platinum and early transition metals as oxygen reduction electrocatalysts,* Nat. Chem., **2009**, 1(7), 552-556

16. Buvat, G.; M.J. Eslamibidgoli; S. Garbarino; M. Eikerling; D. Guay, *OER Performances of Cationic Substituted (100)-Oriented IrO2 Thin Films: A Joint*

Experimental and Theoretical Study, ACS Applied Energy Materials, **2020**, 3(6), 5229-5237

17. Lim, J.; S. Yang; C. Kim; C.-W. Roh; Y. Kwon; Y.-T. Kim; H. Lee, *Shaped Ir–Ni bimetallic nanoparticles for minimizing Ir utilization in oxygen evolution reaction,* Chem. Commun., **2016**, 52(32), 5641-5644
18. Pi, Y.; Q. Shao; P. Wang; J. Guo; X. Huang, *General Formation of Monodisperse IrM (M = Ni, Co, Fe) Bimetallic Nanoclusters as Bifunctional Electrocatalysts for Acidic Overall Water Splitting,* Adv. Funct. Mater., **2017**, 27(27), 1700886
19. Pi, Y.; Q. Shao; X. Zhu; X. Huang, *Dynamic Structure Evolution of Composition Segregated Iridium-Nickel Rhombic Dodecahedra toward Efficient Oxygen Evolution Electrocatalysis,* ACS Nano, **2018**, 12(7), 7371-7379
20. Wang, C.; Y. Sui; M. Xu; C. Liu; G. Xiao; B. Zou, *Synthesis of Ni–Ir Nanocages with Improved Electrocatalytic Performance for the Oxygen Evolution Reaction,* ACS Sustain. Chem. Eng., **2017**, 5(11), 9787-9792
21. Nong, H.N.; H.-S. Oh; T. Reier; E. Willinger; M.-G. Willinger; V. Petkov; D. Teschner; P. Strasser, *Oxide-Supported IrNiOx Xore-Shell Particles as Efficient, Cost-Effective, and Stable Catalysts for Electrochemical Water Splitting,* Angew. Chem. Int. Ed., **2015**, 54(10), 2975 - 2979
22. Nong, H.N.; T. Reier; H.-S. Oh; M. Gliech; P. Paciok; T.H.T. Vu; D. Teschner; M. Heggen; V. Petkov; R. Schlögl; T. Jones; P. Strasser, *A Unique Oxygen Ligand Environment Facilitates Water Oxidation in Hole-Doped IrNiOx Core–Shell Electrocatalysts,* Nat. Catal., **2018**, 1(11), 841-851
23. Xu, S.; S. Chen; L. Tian; Q. Xia; W. Hu, *Selective-leaching method to fabricate an Ir surface-enriched Ir-Ni oxide electrocatalyst for water oxidation,* J. Solid State Electrochem., **2016**, 20(7), 1961-1970

24. Godínez-Salomón, F.; L. Albiter; S.M. Alia; B.S. Pivovar; L.E. Camacho-Forero; P.B. Balbuena; R. Mendoza-Cruz; M.J. Arellano-Jimenez; C.P. Rhodes, *Self-Supported Hydrous Iridium–Nickel Oxide Two-Dimensional Nanoframes for High Activity Oxygen Evolution Electrocatalysts,* ACS Catal., **2018**, 8(11), 10498-10520

25. Reier, T.; Z. Pawolek; S. Cherevko; M. Bruns; T. Jones; D. Teschner; S. Selve; A. Bergmann; H.N. Nong; R. Schlögl; K.J.J. Mayrhofer; P. Strasser, *Molecular Insight in Structure and Activity of Highly Efficient, Low-Ir Ir–Ni Oxide Catalysts for Electrochemical Water Splitting (OER),* J. Am. Chem. Soc., **2015**, 137(40), 13031-13040

26. Papaderakis, A.; N. Pliatsikas; C. Prochaska; G. Vourlias; P. Patsalas; D. Tsiplakides; S. Balomenou; S. Sotiropoulos, *Oxygen Evolution at IrO2 Shell–Ir−Ni Core Electrodes Prepared by Galvanic Replacement,* J. Phys. Chem. C, **2016**, 120(36), 19995-20005

27. Touni, A.; A. Papaderakis; D. Karfaridis; G. Vourlias; S. Sotiropoulos, *Oxygen Evolution Reaction at IrO2/Ir(Ni) Film Electrodes Prepared by Galvanic Replacement and Anodization: Effect of Precursor Ni Film Thickness,* Molecules, **2019**, 24(11), 2095

28. Özer, E.; I. Sinev; A.M. Mingers; J. Araujo; T. Kropp; M. Mavrikakis; K.J.J. Mayrhofer; B.R. Cuenya; P. Strasser, *Ir-Ni Bimetallic OER Catalysts Prepared by Controlled Ni Electrodepostion on Irpoly and Ir(111),* Surfaces, **2018**, 1(1), 165 - 186

29. Gong, L.; D. Ren; Y. Deng; B.S. Yeo, *Efficient and Stable Evolution of Oxygen Using Pulse-Electrodeposited Ir/Ni Oxide Catalyst in Fe-Spiked KOH Electrolyte,* ACS Appl. Mat. Int., **2016**, 8(25), 15985-15990

30. Wang, Q.; X. Huang; Z.L. Zhao; M. Wang; B. Xiang; J. Li; Z. Feng; H. Xu; M. Gu, *Ultrahigh-Loading of Ir Single Atoms on NiO Matrix to Dramatically Enhance Oxygen Evolution Reaction,* J. Am. Chem. Soc., **2020**, 142(16), 7425-7433

31. Zaman, W.Q.; Z. Wang; W. Sun; Z. Zhou; M. Tariq; L. Cao; X.-Q. Gong; J. Yang, *Ni–Co Codoping Breaks the Limitation of Single-Metal-Doped IrO2 with Higher Oxygen Evolution Reaction Performance and Less Iridium,* ACS Energy Lett., **2017**, 2(12), 2786-2793

32. Stoerzinger, K.A.; L. Qiao; M.D. Biegalski; Y. Shao-Horn, *Orientation-Dependent Oxygen Evolution Activities of Rutile IrO2 and RuO2*, J. Phys. Chem. Lett., **2014**, 5(10), 1636-1641

33. Ankudinov, A.L.; B. Ravel; J.J. Rehr; S.D. Conradson, *Real-space multiple-scattering calculation and interpretation of x-ray-absorption near-edge structure,* Phy. Rev. B, **1998**, 58(12), 7565-7576

34. Ressler, T., *WinXAS: a Program for X-ray Absorption Spectroscopy Data Analysis under MS-Windows,* Journal of Synchrotron Radiation, **1998**, 5(2), 118-122

35. Martin, M.H.; J. Galipaud; A. Tranchot; L. Roué; D. Guay, *Measurements of Hydrogen Solubility in CuxPd100−x Thin Films,* Electrochim. Acta, **2013**, 90, 615-622

36. McCrory, C.C.L.; S. Jung; J.C. Peters; T.F. Jaramillo, *Benchmarking Heterogeneous Electrocatalysts for the Oxygen Evolution Reaction,* J. Am. Chem. Soc., **2013**, 135(45), 16977-16987

37. Kresse, G.; J. Furthmüller, *Efficiency of ab-initio Total Energy Calculations for Metals and Semiconductors Using a Plane-Wave Basis Set,* Comput. Mater. Sci., **1996**, 6(1), 15-50

38. Kresse, G.; J. Furthmüller, *Efficient Iterative Schemes for ab initio Total-Energy Calculations Using a Plane-Wave Basis Set,* Phy. Rev. B, **1996**, 54(16), 11169-11186

39. Kresse, G.; J. Hafner, *Ab initio Molecular Dynamics for Liquid Metals,* Phy. Rev. B, **1993**, 47(1), 558-561

40. Kresse, G.; J. Hafner, *Ab initio Molecular-Dynamics Simulation of the Liquid-Metal--Amorphous-Semiconductor Transition in Germanium,* Phy. Rev. B, **1994**, 49(20), 14251-14269

41. Blöchl, P.E., *Projector Augmented-Wave Method,* Phy. Rev. B, **1994**, 50(24), 17953-17979

42. Perdew, J.P.; K. Burke; M. Ernzerhof, *Generalized Gradient Approximation Made Simple,* Phys. Rev. Lett., **1996**, 77(18), 3865-3868

43. Monkhorst, H.J.; J.D. Pack, *Special Points for Brillouin-Zone Integrations,* Phy. Rev. B, **1976**, 13(12), 5188-5192

44. Sen, F.G.; A. Kinaci; B. Narayanan; S.K. Gray; M.J. Davis; S.K.R.S. Sankaranarayanan; M.K.Y. Chan, *Towards accurate prediction of catalytic activity in IrO2 nanoclusters via first principles-based variable charge force field,* Journal of Materials Chemistry A, **2015**, 3(37), 18970-18982

45. Buvat, G.; M.J. Eslamibidgoli; A.H. Youssef; S. Garbarino; A. Ruediger; M. Eikerling; D. Guay, *Effect of IrO6 Octahedron Distortion on the OER Activity at (100) IrO2 Thin Film,* ACS Catal., **2020**, 10(1), 806-817

46. Eason, R., *Pulsed Laser Deposition of Thin Films - Applications-Led Growth of Functional Materials*. 2006: Wiley-Interscience.

47. Poulain, R.; A. Klein; J. Proost, *Electrocatalytic Properties of (100)-, (110)-, and (111)-Oriented NiO Thin Films toward the Oxygen Evolution Reaction,* J. Phys. Chem. C, **2018**, 122(39), 22252-22263

48. Enman, L.J.; M.S. Burke; A.S. Batchellor; S.W. Boettcher, *Effects of Intentionally Incorporated Metal Cations on the Oxygen Evolution Electrocatalytic Activity of Nickel (Oxy)hydroxide in Alkaline Media,* ACS Catal., **2016**, 6(4), 2416-2423

49. Pebley, A.C.; E. Decolvenaere; T.M. Pollock; M.J. Gordon, *Oxygen evolution on Fe-doped NiO electrocatalysts deposited via microplasma,* Nanoscale, **2017**, 9(39), 15070-15082

50. Pfeifer, V.; T.E. Jones; J.J. Velasco Vélez; C. Massué; R. Arrigo; D. Teschner; F. Girgsdies; M. Scherzer; M.T. Greiner; J. Allan; M. Hashagen; G. Weinberg; S. Piccinin; M. Hävecker; A. Knop-Gericke; R. Schlögl, *The electronic structure of iridium and its oxides,* Surf. Interface Anal., **2016**, 48(5), 261-273

51. Kahk, J.M.; C.G. Poll; F.E. Oropeza; J.M. Ablett; D. Céolin; J.P. Rueff; S. Agrestini; Y. Utsumi; K.D. Tsuei; Y.F. Liao; F. Borgatti; G. Panaccione; A. Regoutz; R.G. Egdell; B.J. Morgan; D.O. Scanlon; D.J. Payne, *Understanding the Electronic Structure of ${\mathrm{IrO}}_{2}$ Using Hard-X-ray Photoelectron Spectroscopy and Density-Functional Theory,* Phys. Rev. Lett., **2014**, 112(11), 117601

52. Grosvenor, A.P.; M.C. Biesinger; R.S.C. Smart; N.S. McIntyre, *New interpretations of XPS spectra of nickel metal and oxides,* Surf. Sci., **2006**, 600(9), 1771-1779

53. Nørskov, J.K.; J. Rossmeisl; A. Logadottir; L. Lindqvist; J.R. Kitchin; T. Bligaard; H. Jónsson, *Origin of the Overpotential for Oxygen Reduction at a Fuel-Cell Cathode,* J. Phys. Chem. B, **2004**, 108(46), 17886-17892

54. Diaz-Morales, O.; I. Ledezma-Yanez; M.T.M. Koper; F. Calle-Vallejo, *Guidelines for the Rational Design of Ni-Based Double Hydroxide Electrocatalysts for the Oxygen Evolution Reaction,* ACS Catal., **2015**, 5(9), 5380-5387

55. Petrie, J.R.; V.R. Cooper; J.W. Freeland; T.L. Meyer; Z. Zhang; D.A. Lutterman; H.N. Lee, *Enhanced Bifunctional Oxygen Catalysis in Strained LaNiO3 Perovskites,* J. Am. Chem. Soc., **2016**, 138(8), 2488-2491

56. Wang, L.; K.A. Stoerzinger; L. Chang; X. Yin; Y. Li; C.S. Tang; E. Jia; M.E. Bowden; Z. Yang; A. Abdelsamie; L. You; R. Guo; J. Chen; A. Rusydi; J. Wang; S.A. Chambers; Y. Du, *Strain Effect on Oxygen Evolution Reaction Activity of Epitaxial NdNiO3 Thin Films,* ACS Appl. Mat. Int., **2019**, 11(13), 12941-12947

57. Pesquera, D.; G. Herranz; A. Barla; E. Pellegrin; F. Bondino; E. Magnano; F. Sánchez; J. Fontcuberta, *Surface symmetry-breaking and strain effects on orbital occupancy in transition metal perovskite epitaxial films,* Nature Communications, **2012**, 3(1), 1189

58. Xu, Z.; J.R. Kitchin, *Tuning oxide activity through modification of the crystal and electronic structure: from strain to potential polymorphs,* Phys. Chem. Chem. Phys., **2015**, 17(43), 28943-28949

59. Datta, M.K.; K. Kadakia; O.I. Velikokhatnyi; P.H. Jampani; S.J. Chung; J.A. Poston; A. Manivannan; P.N. Kumta, *High performance robust F-doped tin oxide based oxygen evolution electro-catalysts for PEM based water electrolysis,* Journal of Materials Chemistry A, **2013**, 1(12), 4026-4037

60. Calle-Vallejo, F.; M.T.M. Koper, *First-principles computational electrochemistry: Achievements and challenges,* Electrochim. Acta, **2012**, 84, 3-11

61. Hammer, B.; J.K. Nørskov, *Electronic factors determining the reactivity of metal surfaces,* Surf. Sci., **1995**, 343(3), 211-220

62. Xu, Z.; J.R. Kitchin, *Relationships between the surface electronic and chemical properties of doped 4d and 5d late transition metal dioxides,* J. Phys. Chem. Phys., **2015**, 142(10), 104703

63. M., K.M.T., *Thermodynamic Theory of Multi-Electron Transfer Reactions: Implications for Electrocatalysis*, J. Electroanal. Chem., **2011**, 660(2), 254-260

64. Friebel, D.; M.W. Louie; M. Bajdich; K.E. Sanwald; Y. Cai; A.M. Wise; M.-J. Cheng; D. Sokaras; T.-C. Weng; R. Alonso-Mori; R.C. Davis; J.R. Bargar; J.K. Nørskov; A. Nilsson; A.T. Bell, *Identification of Highly Active Fe Sites in (Ni,Fe)OOH for Electrocatalytic Water Splitting*, J. Am. Chem. Soc., **2015**, 137(3), 1305-1313

Table 1: Nickel composition, thickness, and out-of-plane lattice parameters for the (100) $(Ir,Ni)O_2$ thin films

Nickel content by EDX (at.%)	Thin film thickness by XRR (nm)	Out-of-plane lattice parameter *a* (Å)
0	62.5 ± 3.5	4.4988 ± 0.0001
4 ± 1	60.4 ± 3.5	4.4991 ± 0.0002
15 ± 1	51.8 ± 3.4	4.4684 ± 0.0002

Table 2: The electrochemical active surface area compared to the surface roughness from AFM, and the OER performances of the (100) $(Ir,Ni)O_2$ thin films

Nickel content by EDX (*atm.* %)	RMS roughness from AFM (nm)	Electrochemically active surface area (cm^2)	*j* measured at 1.60 V *vs.* RHE ($\mu A.cm^{-2}_{ox}$)	Overpotential measured at 10 $\mu A.cm^{-2}_{ox}$ (V)
0	1.67	0.525	35	0.341
4	1.54	0.475	102	0.314
15	0.93	0.450	348	0.300

Table 3: Summary of the EXAFS fit parameters for the (100) (Ir,Ni)O_2 films

Nickel content (atm. %)	Scattering path	CN	R (Å)	σ^2 (Å^2)	ΔE_0 (eV)
0	Ir – O	6.0 ± 0.8	1.95 ± 0.01	0.002 ± 0.002	3.7 ± 1.6
4	Ir – O	5.5 ± 0.7	1.96 ± 0.01	0.001 ± 0.002	6.6 ± 1.4
	Ni – O	5.7 ± 0.7	2.03 ± 0.01	0.004 ± 0.002	-7.7 ± 1.2
15	Ir – O	5.5 ± 0.8	1.95 ± 0.01	0.001 ± 0.002	4.2 ± 1.7
	Ni – O	5.0 ± 1.2	2.02 ± 0.02	0.002 ± 0.003	-8.2 ± 2.7

CN is the coordination number; R is bond distance; σ^2 is Debye-Waller factor (a measure of thermal and static disorder in absorber-scatterer distances); ΔE^0 is edge-energy shift (the difference between the zero-kinetic energy value of the sample and that of the theoretical model); amplitude reduction factors of S_0^2 = 0.92 and 0.71 were used for the Ir–O and Ni–O scattering path, respectively (obtained by the fitting of Ir powder and Ni foil).

Table 4: XPS quantification of the Ir and Ni contents, before and after OER, in the (100) (Ir, Ni)O_2 thin films

Nickel content (atm. %)	Before OER		After OER	
	Ir (%)	Ni (%)	Ir (%)	Ni (%)
4	93.7	6.3	92.8	7.2
15	67.2	32.8	67.3	32.7

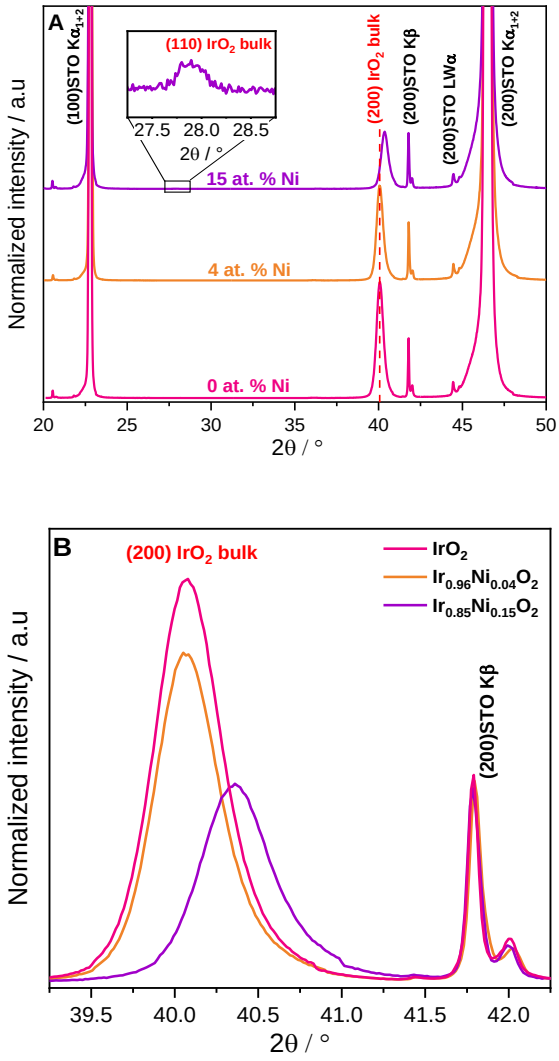

Figure 1: *θ*/2*θ* XRD patterns of (Ir,Ni)O_2 films with different nickel compositions: (A) general view and (B) zoom on the (200) plane of IrO_2. Peak positions of bulk IrO_2 are referenced according to JCPDS file no. 00-015-0870.

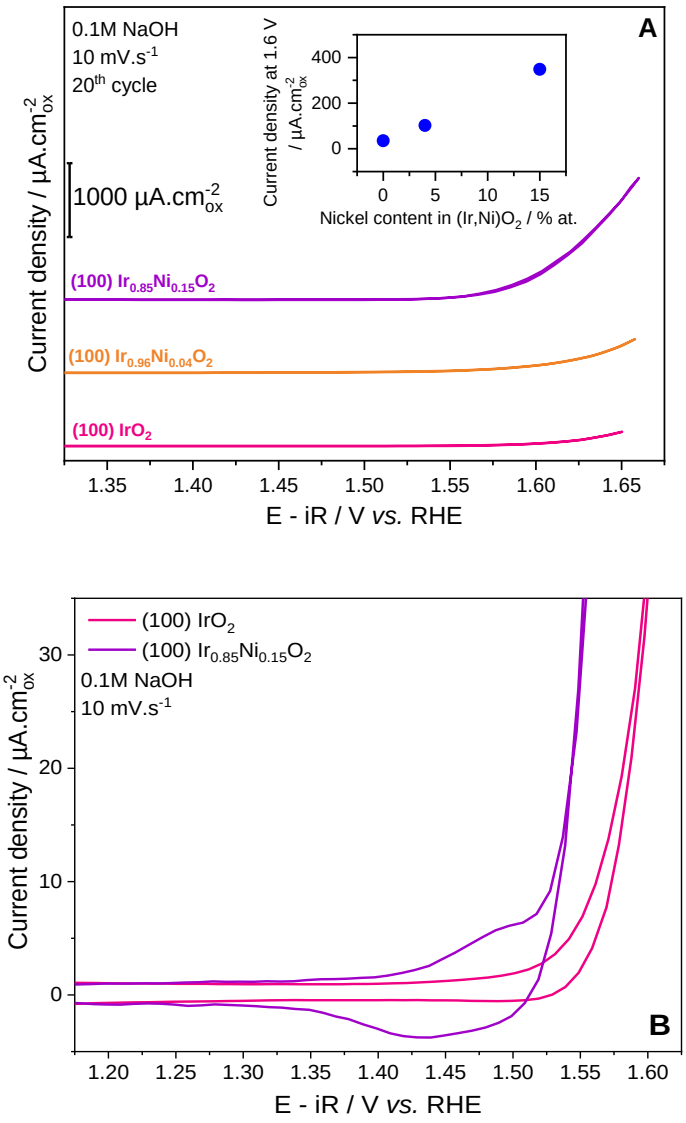

Figure 2: Electrochemical characterization of (100) (Ir,Ni)O_2 thin films, (A) near steady-state cyclic voltammetry in a Ar-saturated 0.1M NaOH electrolyte and recorded at 10 $mV.s^{-1}$, with current density summarized in the inset, and (B) zoom on the columbic charge before the OER wave.

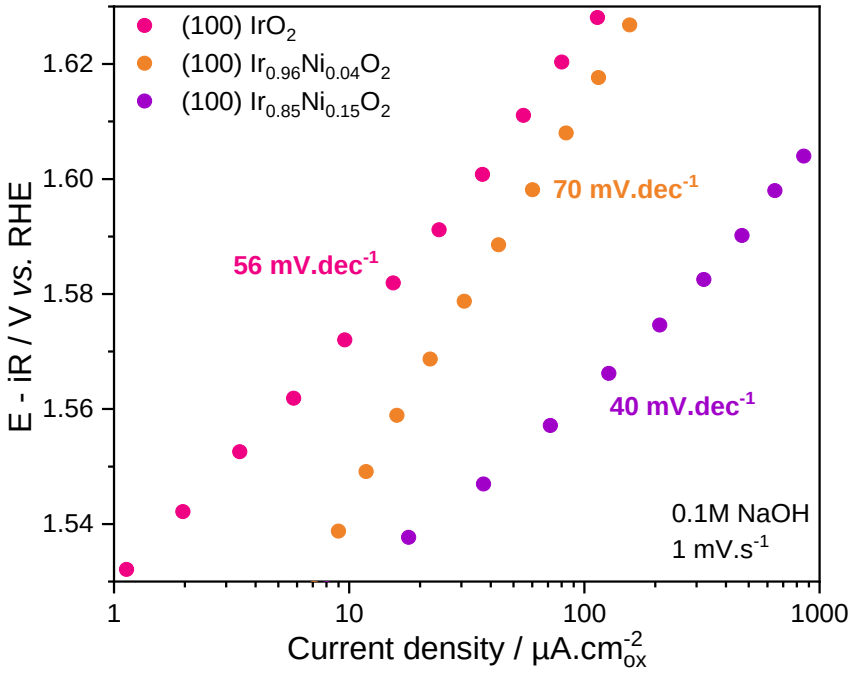

Figure 3: Tafel plots of (100) $Ir_{1-x}Ni_xO_2$ thin films measured by near steady-state cyclic voltammetry with a scan rate of 1 mV s^{-1} in Ar-saturated 0.1 M NaOH electrolyte.

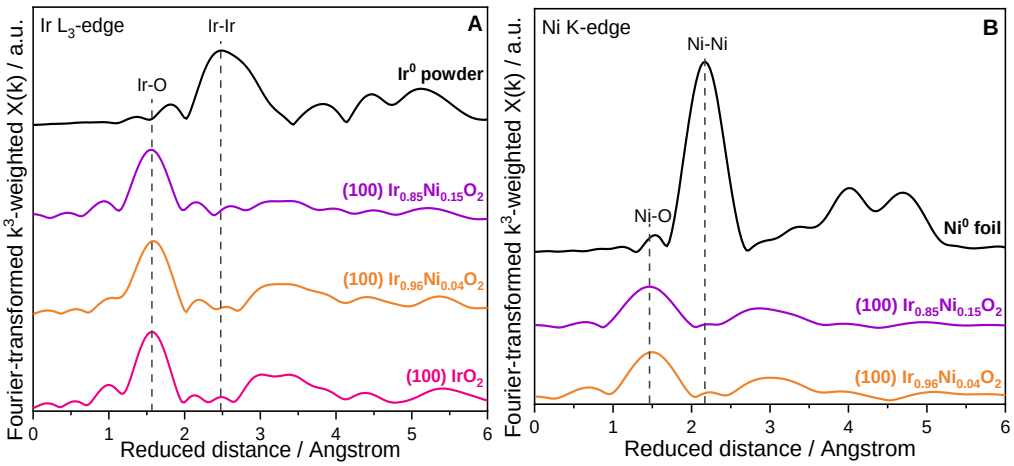

Figure 4: FT-EXAFS of (100)(Ir,Ni)O_2 thin films at the (A) iridium L_3-edge, and (B) nickel K-edge.

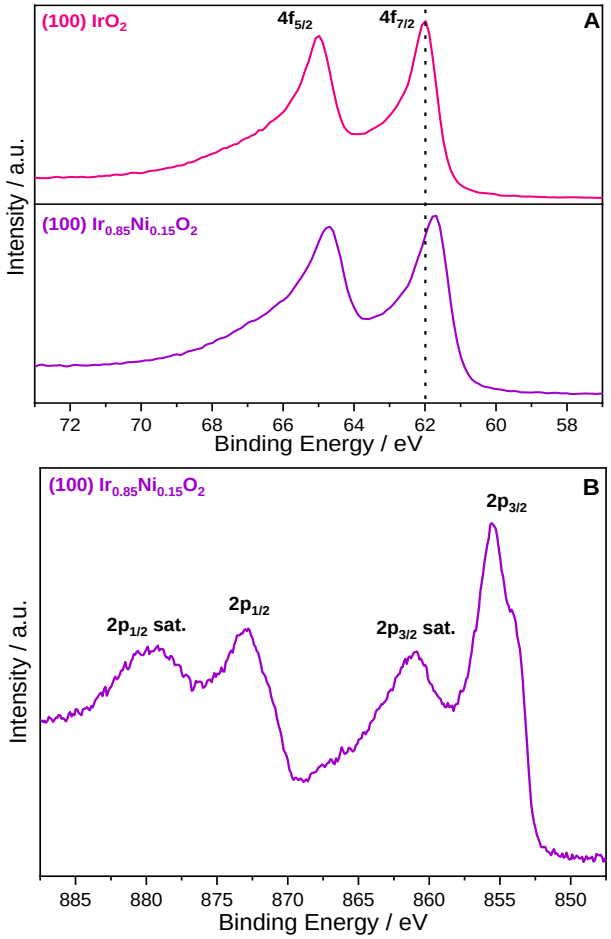

Figure 5: XPS spectra of (100) $Ir_{0.85}Ni_{0.15}O_2$ films measured before OER in the (A) Ir 4f region, and (B) Ni 2p region.

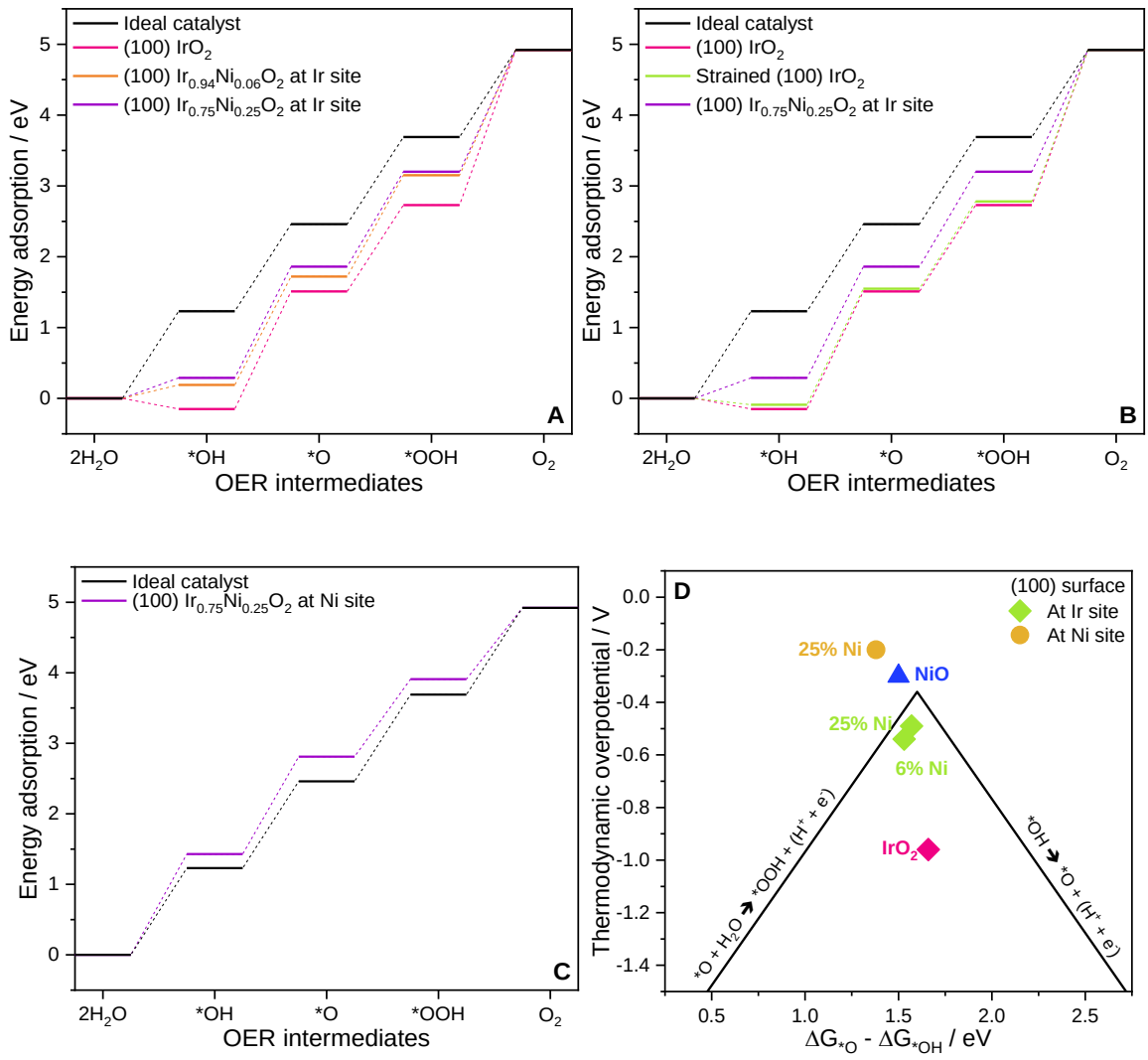

Figure 6: DFT calculation of the adsorption energy of OER intermediates at the (100) surface of $Ir_{1-x}Ni_xO_2$ model slab. In (A), at the iridium site. In (B), on strained IrO_2. In (C), at the nickel site. In (D), thermodynamic overpotential of different $Ir_{1-x}Ni_xO_2$ surfaces with respect to $\Delta G_{*O} - \Delta G_{*OH}$. For comparison, the value for pristine NiO, taken and adapted from ref [54], is also shown.

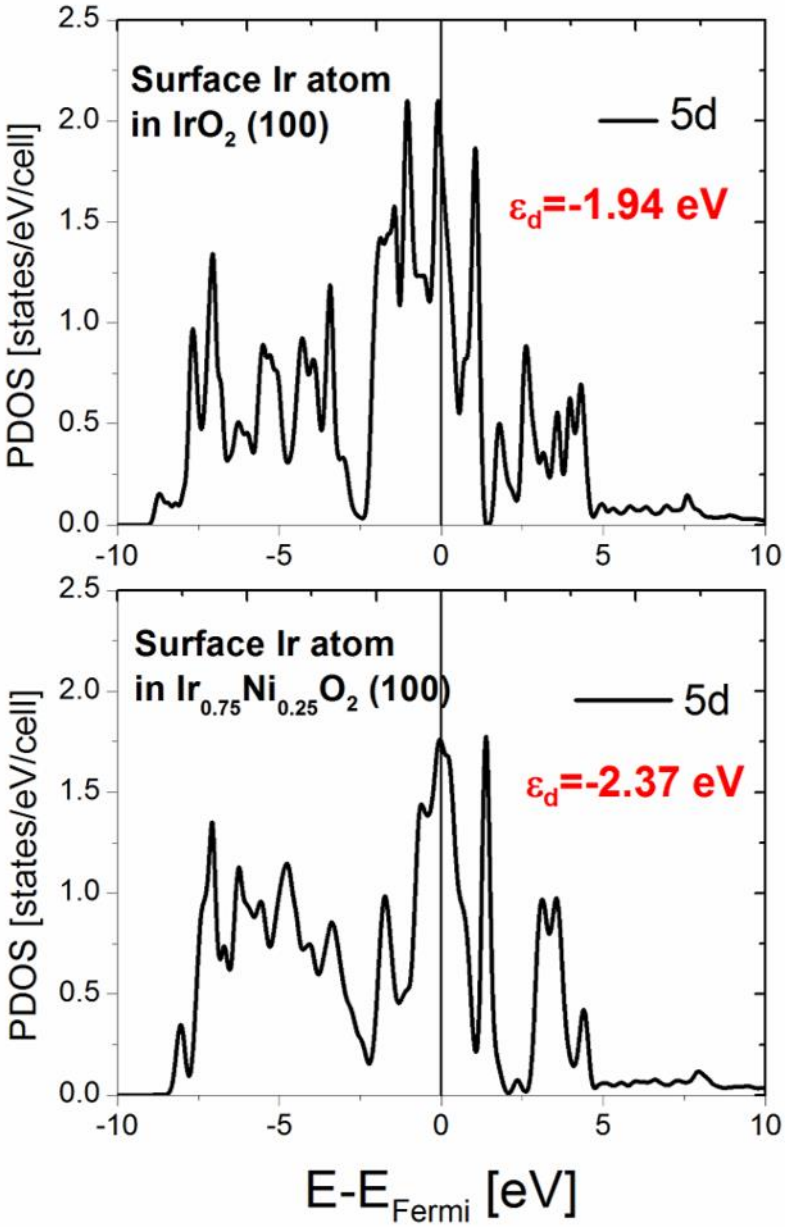

Figure 7: d-projected density of states of surface Ir atoms for (a) (100)-oriented $IrO_2$and (b) (100)-oriented $Ir_{0.75}Ni_{0.25}O_2$.